Journal of Nuclear Materials 563 (2022) 153642

Contents lists available at ScienceDirect

Journal of Nuclear Materials

journal homepage: www.elsevier.com/locate/jnucmat

Combined evaluation of Young modulus and fracture toughness in small specimens of fine grained nuclear graphite using 3D image analysis

Jie Shen[a], T James Marrow[b,*], Daniel Scotson[c], Xiaochao Jin[d,b], Houzheng Wu[e], Hongniao Chen[a,b,*]

[a] Space Structure Research Center, Guizhou University, Guizhou, Guiyang 55002, China
[b] Department of Materials, University of Oxford, Oxford OX1 3PH, United Kingdom
[c] Henry Royce Institute Hub Building, University of Manchester, Manchester M13 9PL, United Kingdom
[d] State Key Laboratory for Strength and Vibration of Mechanical Structures, School of Aerospace Engineering, Xi'an Jiaotong University, Xi'an 710049, China
[e] Department of Materials, Loughborough University, Epinal Way, Loughborough LE11 3TU, United Kingdom

ARTICLE INFO

Article history:
Received 24 October 2021
Accepted 3 March 2022
Available online 10 March 2022

Keywords:
Graphite
Digital volume correlation
Double cleavage drilled compression
Strain energy release rate
Fracture toughness

ABSTRACT

The fracture toughness of the fine-grained nuclear graphite SNG742 has been investigated by observation of stable crack propagation in double cleavage drilled compression specimens. The three-dimensional displacement fields were obtained by digital volume correlation (DVC) of in situ laboratory X-ray computed tomographs. The crack tip location and crack opening displacements were determined using an image edge detection algorithm based on the wavelet modulus maxima. The Young modulus was estimated by fitting a finite element model to DVC displacement field data measured before crack initiation. Using the 3D crack geometry and the surrounding full-field 3D displacement fields as boundary conditions, the elastic strain energy release rate J and the three-dimensional stress intensity factors K_I to K_{III} were then evaluated via the contour integral method. Constant mode I critical stress intensity factor was obtained along the curved crack fronts, with negligible shearing modes. This method allows evaluation of the fracture toughness without prior knowledge of elastic properties, and has potential applications to assess the effects of high temperature, oxidation and irradiation in small specimens of nuclear graphite.

1. Introduction

Graphite is important for high temperature gas reactors (HTGR) because of its good neutron moderation, high temperature resistance and high radiation resistance [1,2]. HTGR graphite components must sustain loading from self-weight, mechanical forces, thermal and radiation stresses and seismic activity [3], which may be sufficient to initiate and propagate fracture [4–7]. The fracture properties of graphite must therefore be considered in the design process to predict failure and ensure the safe operation of HTGRs [8–11]. The fracture properties of unirradiated nuclear graphite are obtained from standardized samples [12]. However, data for irradiated graphite requires material to be either obtained by extraction (e.g. trepanning) from a working reactor or by irradiation in a material test reactor, which both impose significant limits on the specimen dimensions [13,14]. To obtain stable crack growth in small specimens of irradiated graphite to measure the fracture resistance, the double cleavage drilled compression (DCDC) specimen [15] has been proposed [16].

The DCDC specimen, first used by Janssen to study fracture of glass [17], is a centimetre scale cuboid with a through-thickness hole in the center. When loaded axially under compression, tensile stresses develop at the hole due to the Poisson effect. Aided in some DCDC geometries by axial notches that extend from the hole, these tensile stresses lead to initiation and stable propagation of axial, through-thickness cracks [15,18].

Various analytical solutions for the stress intensity factor in a DCDC specimen have been developed [18,19], from which the critical mode I stress intensity factor (i.e. fracture toughness) can be obtained using the critical load for quasi-static propagation of cracks of known dimensions. However, these solutions have some limitations. In small specimens, due to frictional and constraint effects and also possible misalignments and residual stresses, the assumed applied boundary conditions of the analytical solution may not be satisfied [20,21]. Recently, an alternative approach has been

* Corresponding authors at: Department of Materials, University of Oxford, Oxford OX1 3PH, United Kingdom.
E-mail addresses: james.marrow@materials.ox.ac.uk (T.J. Marrow), hqchen@gzu.edu.cn (H. Chen).

https://doi.org/10.1016/j.jnucmat.2022.153642

developed that allows the crack tip stress intensity factor to be determined using the measured full-field displacements [20,21,22] as local boundary conditions.

In previous studies of graphite fracture, the full-field displacements have been measured by digital image correlation (DIC) [23] and laser-based ESPI (electronic speckle pattern interferometry) method [24,25]; however, these can only observe surface deformation. To obtain the internal three-dimensional displacement field, digital volume correlation (DVC) of in situ X-ray computed tomographs (XCT) can be employed [22,26]. In the DVC technique, the attenuation contrast from the inhomogeneity of the microstructure (i.e. porosity) provides the necessary speckle for image correlation [27,28]. In a recent study, crack propagation behavior of unirradiated and irradiated investigated Gilsocarbon graphite was examined using DCDC specimens [22]. The measured 3D displacement fields were used to detect the crack tip and to obtain the critical mode I stress intensity factor for crack propagation. However, although tomography showed the crack front was curved, for simplicity the analysis for the stress intensity factor assumed a straight curve front. Curved cracks may also lead to errors in analyses that only use surface displacement fields measured by DIC, so it is important to understand their effect.

Knowledge of the elastic properties is required to calculate the strain energy release rate and stress intensity factor in brittle materials. In most engineering materials, the elastic (Young) modulus is a constant that only changes with temperature and can be easily evaluated in representative specimens. In coarse grained graphite, such as Gilsocarbon, the Young modulus is quite non-linear [29] in the unirradiated condition, but it has been shown that the elastic strain energy release rate can be correctly obtained by analysis of the displacement field with a suitable calibration of the non-linear stress/strain relationship [20]. Fine-grained graphites also show some non-linearity in the unirradiated state, though to a lesser degree [30]. Importantly, radiation and oxidation in nuclear reactors change the internal microstructure of graphite with consequent effects on the elastic properties [31,32–34]. For instance, fast neutron irradiation increases the Young modulus and also removes its non-linearity, whereas radiolytic oxidation can significantly decrease the Young modulus (Poisson ratio is less affected by irradiation [2]). It is therefore critical to know the Young modulus of the test specimen. This may be estimated from knowledge of the material's irradiation and oxidation history, or measured by testing of similar material that experienced the same history; however, both of these can be subject to uncertainties or limited availability of data or material. Small specimens may also be affected when there is significant spatial heterogeneity in the properties of the bulk graphite material [35–37]. Ideally, the elastic properties should be measured in the same specimen that is used for fracture testing, but the specimen geometry requirements for standard tests of modulus and fracture toughness differ significantly. One approach to achieve this is inverse modeling [38,39], using the measured displacement fields and the boundary conditions of the specimen geometry and applied loading to extract the elastic properties directly [30].

In this paper, inverse modeling has been applied to obtain the Young modulus of graphite in a DCDC specimen that is subsequently tested to measure the fracture toughness (i.e., the critical mode I stress intensity factor, K_{Ic}, for quasi-static crack propagation). The material is a fine grained graphite (SNG742) with potential application in HTGR [40]. The three-dimensional displacement field, measured by DVC of laboratory XCT images obtained during in situ loading of an undamaged specimen, has been compared with numerically simulated elastic displacements to estimate the Young modulus. After further loading to initiate and propagate stable fracture, the 3D shapes of cracks were measured by an image edge detection algorithm based on wavelet modulus maxima. Using the measured displacement field as local boundary conditions, the elastic strain energy release rate, J, and the three-dimensional stress intensity factors, K_I to K_{III}, were determined by contour integral and interaction integral methods implemented in linear elastic finite element models that replicated the curved crack front. The sensitivity of the result to the estimated Young modulus was also evaluated. The objectives were to demonstrate there was a constant crack field along the 3D crack tip that described the critical condition for quasi-static crack propagation, and also to evaluate the errors introduced by neglecting the crack front curvature. The methodology demonstrated here is proposed to be suitable for evaluating the fracture toughness in small specimens of unknown elastic properties, such as irradiated and oxidized graphite at elevated temperatures.

2. Experiment and analysis methods

2.1. Materials and experiment

SNG742, produced by Sinosteel Ltd. (Beijing, China), is a candidate graphite material for next generation nuclear energy [40] with a fine grain size (coke size ~20 μm [41]). The geometry of the DCDC specimen ($X \times Y \times Z$) is 7 × 20 × 7 mm. A central through-thickness hole (2 mm diameter) aligned with the Z-direction was prepared with a central axial notch of 1 mm length and 0.5 mm width extending above and below the hole (Fig. 1a). Uniaxial compression loading was applied to the specimen using a 5 KN Deben CT5000 H250, with an X-ray transparent glassy carbon load-bearing tube, which was installed in a Zeiss Xradia 510 Versa X-ray microscope (Fig. 1b). X-ray computed tomography scans were obtained at three loading stages: pre-loading (~20 N), 1116 N and 2000 N that corresponded to i) reference state, ii) uncracked state (~23 MPa compression) and iii) cracked state (~ 41 MPa compression) of the specimen, respectively. Each tomograph was obtained with 1601 radiographic projections over a full 360º rotation, each with a field of view of 11.7 × 11.7 mm (2008 × 2020 pixels at an effective pixel size of 5.81 μm), with 40 s exposure time per radiograph (60 kV and 5 W power). The tomographic images were reconstructed using the Zeiss' Scout-and-Scan software.

2.2. Digital volume correlation (DVC) analysis

DVC analyses were performed using the LaVision DaVis software (version 8.4.0) and were conducted with the tomographic image at the pre-loaded state as the reference. A procedure that combined an initial FFT (Fast Fourier Transform) correlation and then a series of multi-pass direct correlations was applied.

For the specimen in the loaded and uncracked state (P = 1116 N), the DVC analysis was performed using a large subset size of 64 × 64 × 64 voxels after the tomographs were cropped to dimensions (X × Y × Z) of 1200 × 664 × 1144 voxels (6.97 × 3.86 × 6.65 mm). The DVC analysis used four passes with a starting subset size of 192 × 192 × 192 voxels. When the specimen was in the loaded and cracked state (P = 2000 N), a higher spatial resolution analysis with a small subset size of 8 × 8 × 8 voxels was used to aid identification of the crack tip with the tomographs cropped to dimensions (X × Y × Z) of 112 × 320 × 1144 voxels (0.65 × 1.86 × 6.65 mm) around the crack. The subsequent DVC analysis used four passes with a starting subset size of 64 × 64 × 64 voxels. A large subset (64 × 64 × 64 voxels) pass was also used to obtain the boundary conditions for the numerical analysis of the J-integral and stress intensity factor, with the tomographs cropped to dimensions (X × Y × Z) of 1200 × 664 × 1144 voxels (6.97 × 3.86 × 6.65 mm) around the crack.

For all analyses, an overlap of 75% between subsets was adopted and each cropped tomograph observed the full thickness

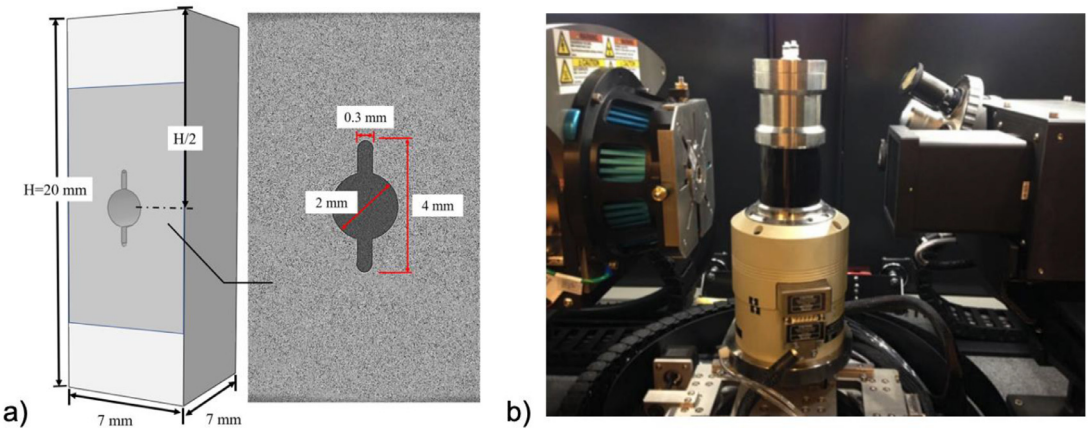

Fig. 1. (a) Geometric dimensions of DCDC specimen and an example XCT image (2D slice of 3D reconstruction); (b) Experimental setup of compressive test in the Deben CT5000 loading rig (center) between the X-ray source (left) and detector (right).

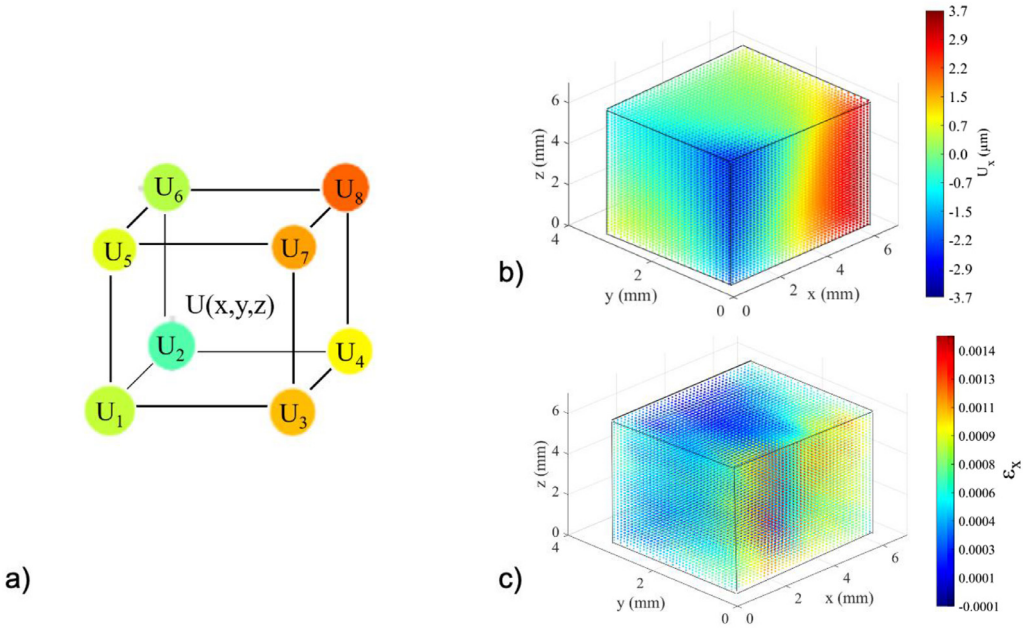

Fig. 2. 3D displacement field and strain field–(a) A set formed of eight nodes; (b) 3D displacement field measured by DVC; (c) 3D strain field measured by DVC.

of the test specimen. Before each DVC analysis, the two tomographs were manually registered (integer voxel precision) to remove rigid body translations, and sub-voxel registration was done in the DVC analysis. A parameter analysis found that the influence of subset sizes on the DVC results was slight, and the standard deviation of the mean transverse displacement (i.e. a measure of the uncertainty in the displacement vector magnitude) in regions remote from the stress concentration of the hole was $\sim 0.18\ \mu$m. The correlation was good, with values in all DVC analyses close to 1.

To transform the displacement fields into strain fields, a displacement function $U(x,\ y,\ z)$ was acquired by interpolating sets, defined by eight adjacent nodes, according to the Lagrange interpolation formula (Fig. 2a). The strain field inside the set was obtained by calculating the partial derivative of the displacement function. As an example, Fig. 2b shows a section of the 3D displacement field obtained at $P = 1116$ N and its strain field is shown in Fig. 2c.

2.3. Edge detection of the crack

Phase congruency has been applied previously to detect cracks by identifying the discontinuity in the displacement field [22,42,43]. Here, we apply an alternative edge detection algorithm that is based on the wavelet modulus maximum. This is a common algorithm for edge detection in images [44,45]. The image in this case is the displacement field. The basic principle of the edge detection algorithm is as follows: (1) Using the Gaussian function as a smoothing function to remove image noise, the first derivative of the smoothing function is taken as the wavelet function to transform the image; (2) the modulus and phase angle of the wavelet transform vector are calculated; (3) the modulus maxima can be found along the direction of the phase angle and its position is regarded as the edge.

Although image noise might be identified as the modulus maxima, the wavelet coefficients' amplitude of the noise was smaller than that of the edge points used to define the crack, Therefore, noise could be filtered out with an appropriate threshold. The algorithm is limited to 2D image analysis, so the 3D displacement field in the X-direction (U_x) was analyzed as a series of X-Y plane slices using an $8 \times 8 \times 8$ voxel subset size assessed to determine the crack tip position and length in each slice. The data from all the slices were then combined to define the 3D crack shape.

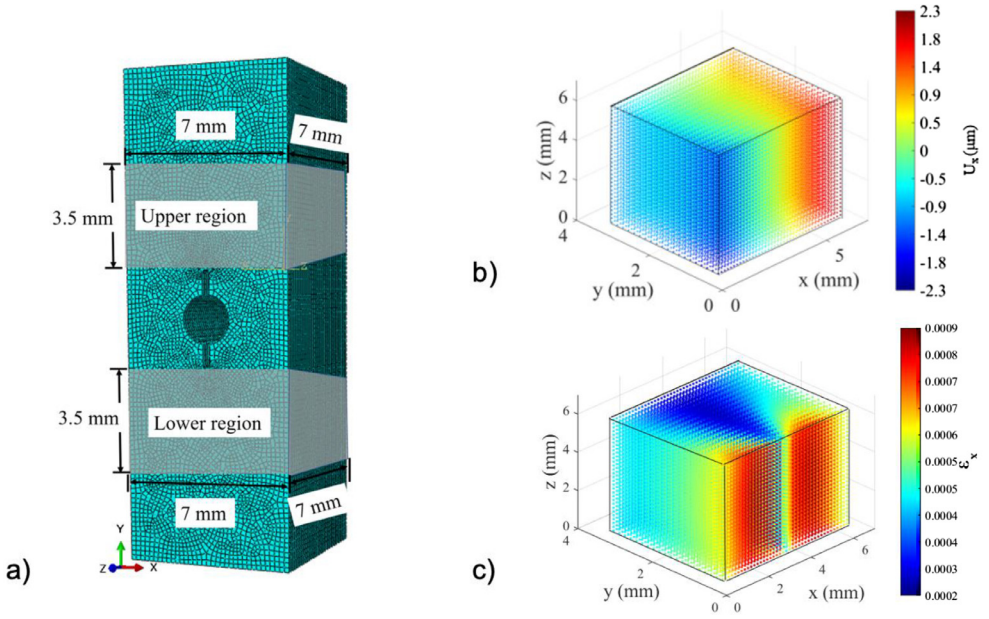

Fig. 3. 3D finite element model of uncracked state (P = 1116N)–(a) Finite element mesh; (b) Numerical displacement field of the analyzed upper region; (c) Numerical strain field of the analyzed upper region.

2.4. Finite element analysis

2.4.1. Estimation of Young modulus

A 3D finite element model (FEM) was created in Abaqus 6.14 to simulate the uncracked state (P = 1116 N) of the specimen. Through establishing this numerical model with the same geometry as the graphite specimen, the Young modulus of graphite was determined inversely by comparing the FEM with the DVC displacements. For the model, a homogeneous material with linear elastic properties and Poisson's ratio = 0.2 was assumed. Hexahedral solid elements were also used, with a mesh size of 0.2 mm, resulting in 201,355 elements and 213,624 nodes in total (Fig. 3a). The Y-direction displacement of the lower end of the model was restrained and a uniform load of 1116N was applied to the upper end. To allow direct comparison, the displacement and strain field outputs of the FEM (Fig. 3b and Fig. 3c) were interpolated to obtain values at the locations of the DVC nodes.

2.4.2. Evaluation of fracture toughness

The elastic strain energy release rate, J, was calculated numerically by evaluating the J-integral in a FEM that simulated the cracked stage (P = 2000 N) of the specimen. Two cracked regions (upper region and lower region in Fig. 3a) were studied, with these cracks having propagated from the notches above and below the hole. To reduce the computing time, a model size of (X × Y × Z) 2 × 2.5 × 6.7 mm was considered in the FE simulation (Fig. 4a). The model was divided into two regions: the boundary condition (BC) region and a free region (i.e. no nodal displacements were imposed within the free region and the crack is a free surface). In the BC region, the full-field displacements of the DVC analysis that used a subset size of 64 × 64 × 64 voxels were applied to the nodes as boundary conditions (linear interpolation was used to obtain nodal displacements where there were no data). The displacements and strains in the free region around the crack were calculated by the FEM, as shown in Fig. 4b and Fig. 4c. The values of J along the crack tip were determined by the contour integral method that is natively implemented in the Abaqus software. The three-dimensional stress intensity factors, K_I, K_{II} and K_{III}, were then obtained at all points along the crack tip, using the interaction integral within Abaqus.

3. Results and discussion

3.1. Displacement field

The FEM for determining the Young modulus assumed uniform loading, and comparison of the FEM displacement field (Fig. 3b) with the DVC results (Fig. 2b) shows the symmetry of the numerical simulation is not quite obtained in the specimen, which may be due to slight misalignment of the loading anvils or non-parallel surfaces of the test specimen. The middle section of the specimen (z = 3.5 mm) was selected for the following analysis, and the displacement and strain fields obtained by DVC and FEM are shown in Fig. 5. Here there is good agreement between the displacement fields (Fig. 5a and Fig. 5b). The strain fields (Fig. 5c and Fig. 5d) also agree well, with some local effects that are judged to be from measurement noise but may also show that the graphite is not truly homogeneous [29].

The strain concentration at the notch is more significant in the DVC results than the FEM simulation. This is attributed to the assumption of linear elastic properties in the FEM, whereas larger strains may develop at the stress concentration due to the nonlinear properties of graphite. Differences in the notch geometry between the model and the machined notch may also contribute, as might the effects of mechanical damage from cutting of the notch, but these would be quite local to the notch tip and so are judged to be less significant.

3.2. Evaluation of the Young modulus

The Young modulus of graphite was estimated by comparing the numerical displacements in the X-direction with the DVC results. For all the points on a horizontal line with the same Y coordinates, displacement vectors in the X-direction were extracted from both the DVC and FEM displacement fields(Fig. 6a), and linear fits were applied to determine the gradient (i.e., the effective average strain in the X-direction as a function of Y). In the FEM,

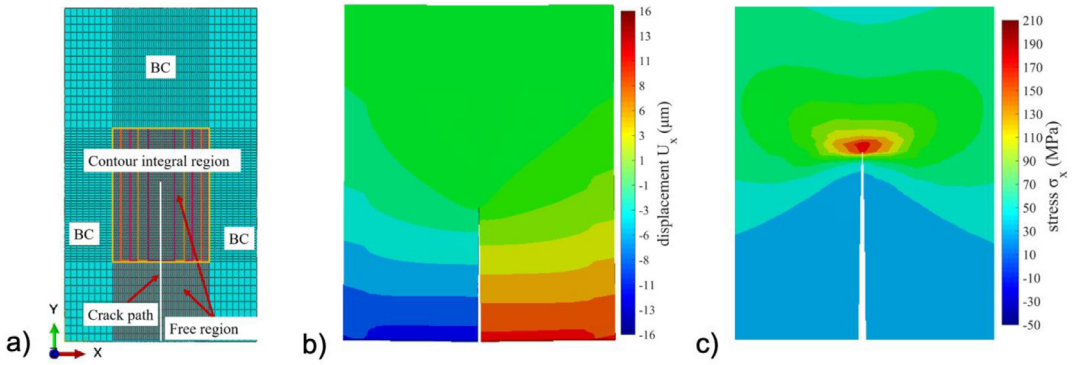

Fig. 4. Finite element analysis using the DVC-measured displacement field as boundary conditions–(a) Finite element model with different regions labelled; (b) Displacement field on X-Y plane ($z = 0$ mm); (c) Strain field (ε_x) around crack tip on X-Y plane ($z = 0$ mm).

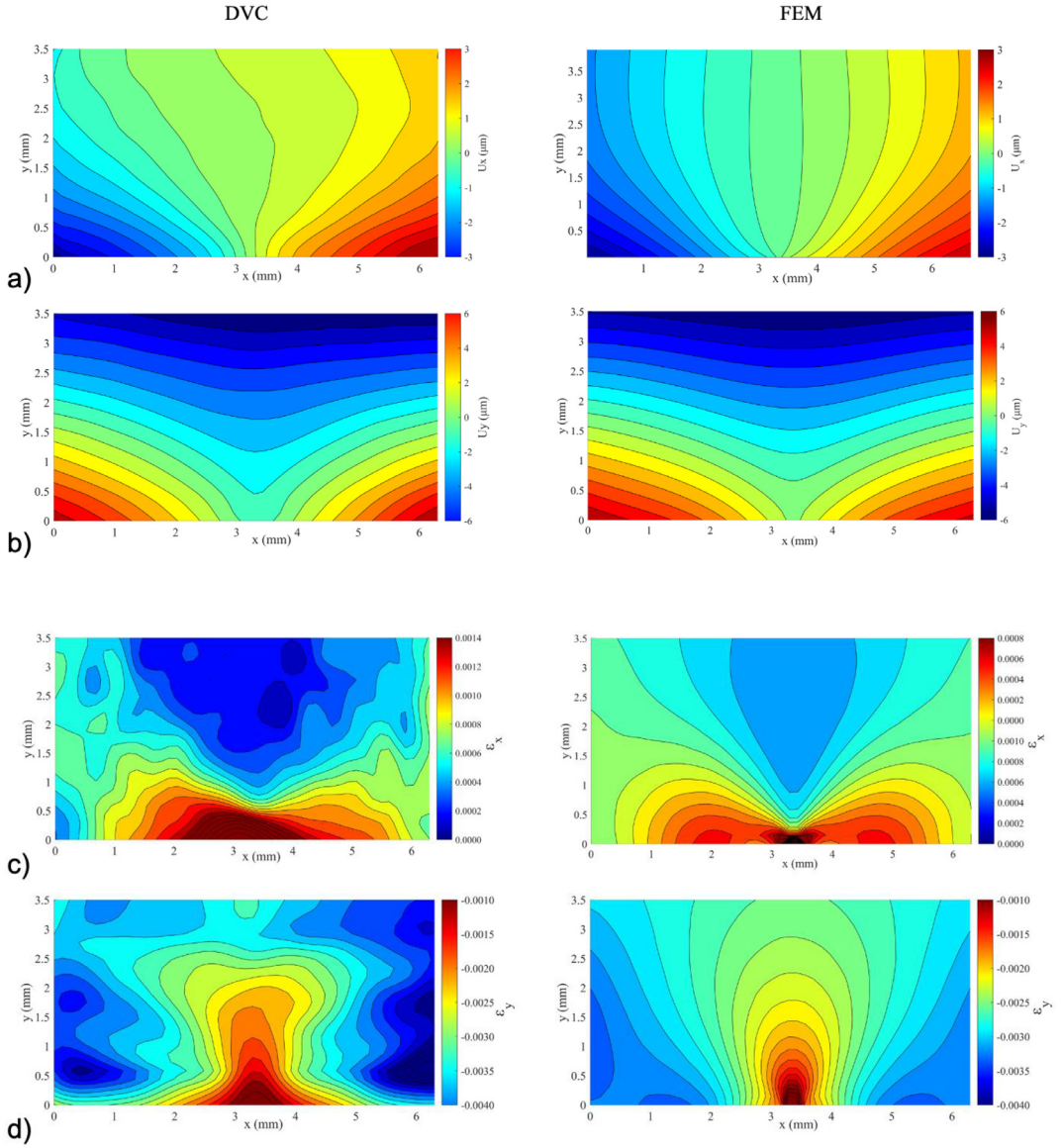

Fig. 5. Comparison of displacement and strain contours from DVC and FEM ($z = 3.5$ mm). Load, $P = 1116$N–a) Displacement contours in X-direction; b) Displacement contours in Y-direction: c) Strain contours in X-direction; Strain contours in Y-direction.

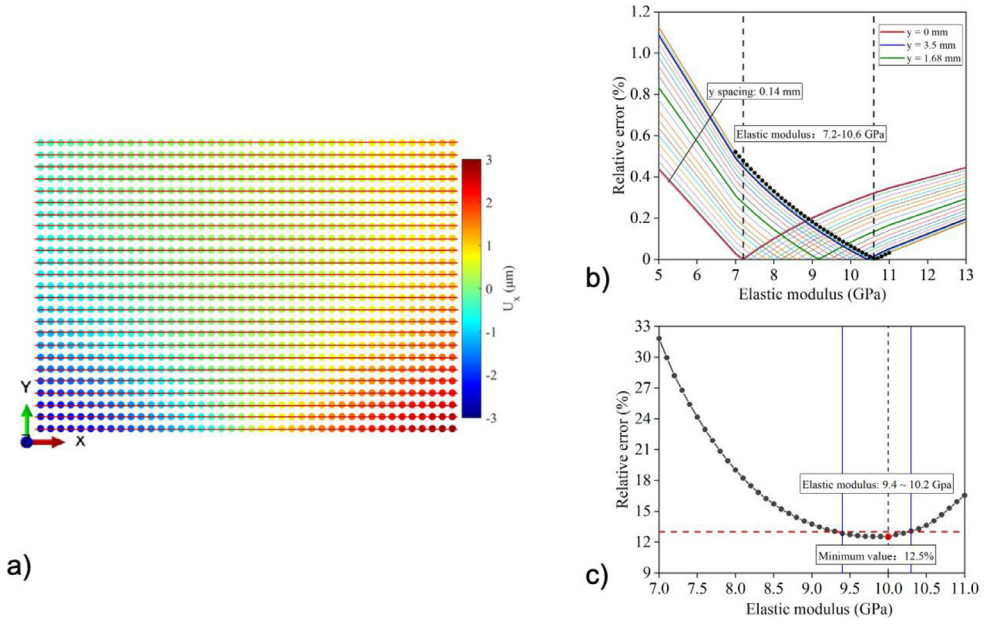

Fig. 6. The estimation of Young modulus–(a) Schematic diagram of displacement vectors on horizontal lines; (b) Gradient errors of each horizontal line with Young modulus intervals of 0.1 GPa; (c) Average gradient error of all horizontal lines.

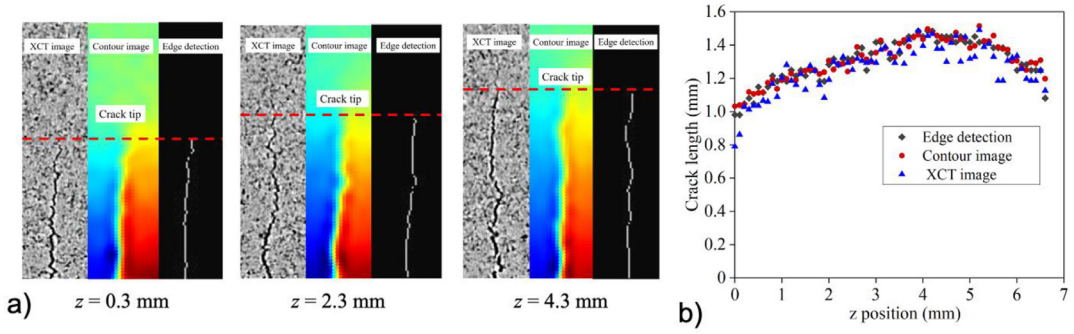

Fig. 7. Identification of crack length in the upper region–(a) Crack paths detected from XCT, displacement contour and edge detection images (red dashed line indicates the position of crack tip); (b) Crack lengths along the thickness direction.

this was performed for a range of assumed Young modulus and the gradients were compared between the DVC data to obtain the relative errors (Fig. 6b and Fig. 6c).

The errors were lower for Young moduli between 7.2 GPa to 10.6 GPa (Fig. 7a). By considering the average error (Fig. 7b), the moduli between 9.4 ~ 10.2 GPa have an error lower than 13% and the minimum average error was 12.5% when the Young modulus was 10 GPa. This is close to the nominal Young modulus of SNG742, which is 11 GPa [40]. The optimal value of 10 GPa was used in the following assessment of the fracture toughness.

The lower Young modulus obtained here may be due to neglect of the contribution of non-linear effects at higher strains closer to the notch. For irradiated graphite, the non-linearity commonly observed in unirradiated graphite is removed [2], and the errors in this simple analysis caused by ignoring the non-linearity would be reduced. In conditions where more significant non-linearity might occur (e.g. high temperatures, low irradiation dose or significant oxidation), the Young modulus could be determined by more advanced inverse modeling, such as the double iterative finite element model updating (FEMU) technique with artificial neural networks (ANNs) [30].

3.3. Crack characterization

The crack tip and crack length were determined from DVC displacement field using the image edge detection algorithm based on wavelet modulus maxima. The crack paths were also identified manually from XCT images and by inspection of the displacement field images. Their comparison (Fig. 7 shows a section of the upper region as an example) shows the crack paths obtained by the three methods were quite consistent. The crack front identified directly from the XCT images fluctuates, and this may be due to subjective errors in judging the crack tip position against the varying contrast of the porous microstructure. It may also indicate local heterogeneities in material properties that locally retard or extend the crack. The crack front that was detected objectively by the edge detection method was used in the estimation of fracture toughness, since this is directly connected to the displacement field that determines the strain energy release rate of crack propagation within the specimen, and also is measured at a length scale that is greater than the microstructural heterogeneity.

The mode I crack opening displacement (COD) in the upper region, obtained using the large subset (64 × 64 × 64 voxel) DVC

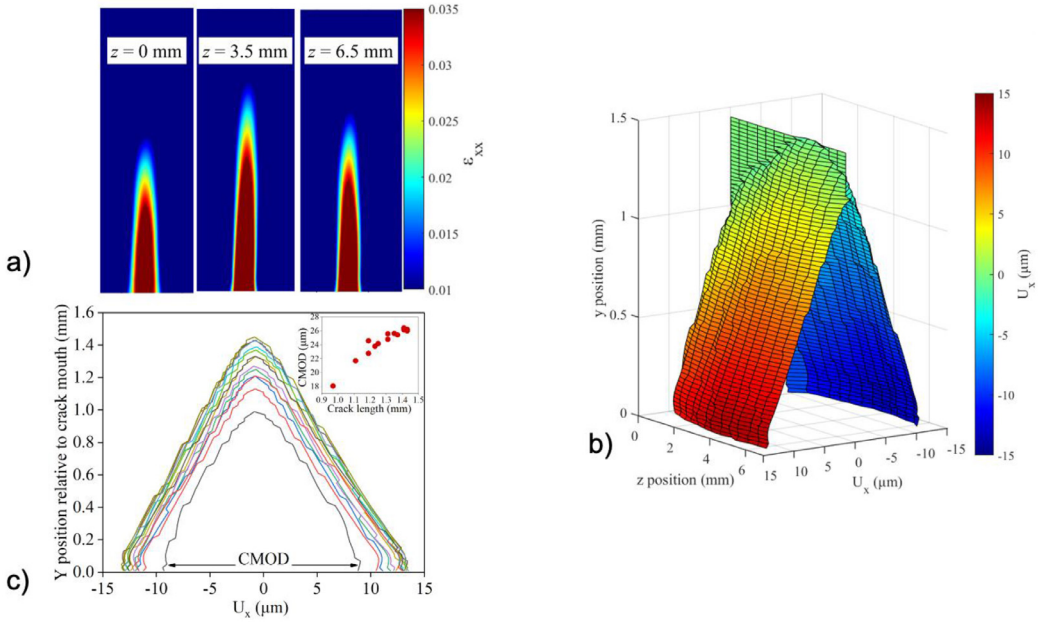

Fig. 8. Crack opening of the upper crack–(a) X-direction strain concentration regions (64×64×64 voxel DVC subset) used to define the location of COD (crack opening displacement); (b) 3D plot of the COD; (c) COD curves measured at different X-Y sections along the crack front, and (inset) the relation between crack length and CMOD (crack mouth opening displacement).

data, is shown in Fig. 8. First, the region with a concentration of X-direction strain was identified (Fig. 8a), then the COD was determined from the relative difference between the X-direction displacements on either side of the strain concentration region (Fig. 8b) Fig. 8c shows how the COD profile varied across the thickness (Z-axis) of the specimen. The crack length, measured from the crack mouth, varied by about 0.5 mm across the specimen width due to the curvature of the crack front. The crack opening mouth displacement (CMOD) was measured at the notch tip, and there was a linear trend between the CMOD and crack length. The crack tip opening angle was 1.5 ± 0.0°.

3.4. Fracture toughness evaluation

Two different measures of the crack front were considered to evaluate the benefit of including crack curvature. The first used a smooth fit of the curved crack identified by the edge detection algorithm (Fig. 9a). The second assumed a straight crack front across the specimen with the average crack length (1.31 mm and 1.22 mm for the upper and lower regions respectively).

To assess the sensitivity of the contour integral to the size of the free region, five regions with different size were evaluated (defined in Fig. 4a). A representative example, for the XY plane at $Z = 3.5$ mm in the upper region (Fig. 9b), shows this region size has a negligible influence. Hence, using the average of the five regions, the mode I, mode II and mode III stress intensity factors along the crack front were calculated for both curved and straight crack fronts (Fig. 9c and Fig. 9d). For the curved crack front, the mode I stress intensity factor K_I was quite constant along the crack front, with average of 1.47 ± 0.05 MPa $m^{1/2}$ for the upper crack and 1.27 ± 0.05 MPa $m^{1/2}$ for the lower crack respectively. The shear modes of stress intensity factor, K_{II} and K_{III}, were both very low, with average values of 0.08 ± 0.11 and 0.02 ± 0.02 MPa $m^{1/2}$ for the upper crack and −0.03 ± 0.08 and 0.04 ± 0.01 MPa $m^{1/2}$ for the lower crack respectively, indicating mode-I loading has been achieved in the DCDC specimen geometry. There is no significant effect of the crack length, as shown in Fig. 9e. The cracks propagated in a stable manner, so the mode I stress intensity factor represents the critical condition at the crack tip and is thus a measure of the fracture toughness, K_{Ic}. R-curve behavior has been reported in large graphite specimens [25] in which the fracture resistance rises with the increasing crack length, but the extent of crack growth in this study is insufficient to evolve toughening mechanisms such as crack branching and bridging. Similar constant toughness with crack length has been observed in a small DCDC specimen of Gilsocarbon graphite [22]. The value of K_{Ic} of the lower crack is slightly less than that of the upper crack. This difference may be due to the heterogeneity of the material, since the measurements are made over a quite small length scale.

The average values of the critical mode I stress intensity factor are higher than the expected fracture toughness of SNG742 graphite, which is reported to be 1.12 MPa $m^{1/2}$ [41]. This is due to the assumption of linear elasticity. As noted above, the non-linear deformation at the high stresses close to the crack tip will increase the displacements that are measured around the crack, with a consequent over-estimate of the elastic strain energy release rate [22]. More accurate values could be obtained with a suitable non-linear property model in the FEM that is used to calculate the J-integral, and also in irradiated graphite where the deformation is more linear.

For the straight crack front, K_I varied over the thickness, with lower values close to the surface where the averaged crack length was longer than the true value. This has also been observed previously in thinner DCDC graphite specimens [22]. Nonetheless, the average K_I of the upper and lower cracks of 1.50 ± 0.24 MPa $m^{1/2}$ and 1.34 ± 0.17 MPa $m^{1/2}$ respectively are quite close to the values obtained using the curved crack front. Hence, while the straight crack front approximation may cause some error, for the level of curvature experienced in this study its average is sufficiently accurate.

To evaluate the effect of uncertainty in the Young modulus, the stress intensity factors obtained with different Young modulus were calculated. Results for the upper crack, presented in Fig. 9e, show that as the modulus varied from 9 GPa to 11 GPa, the average mode I stress intensity factor K_I for the curved crack increased linearly from 1.32 to 1.61 MPa.$m^{1/2}$.

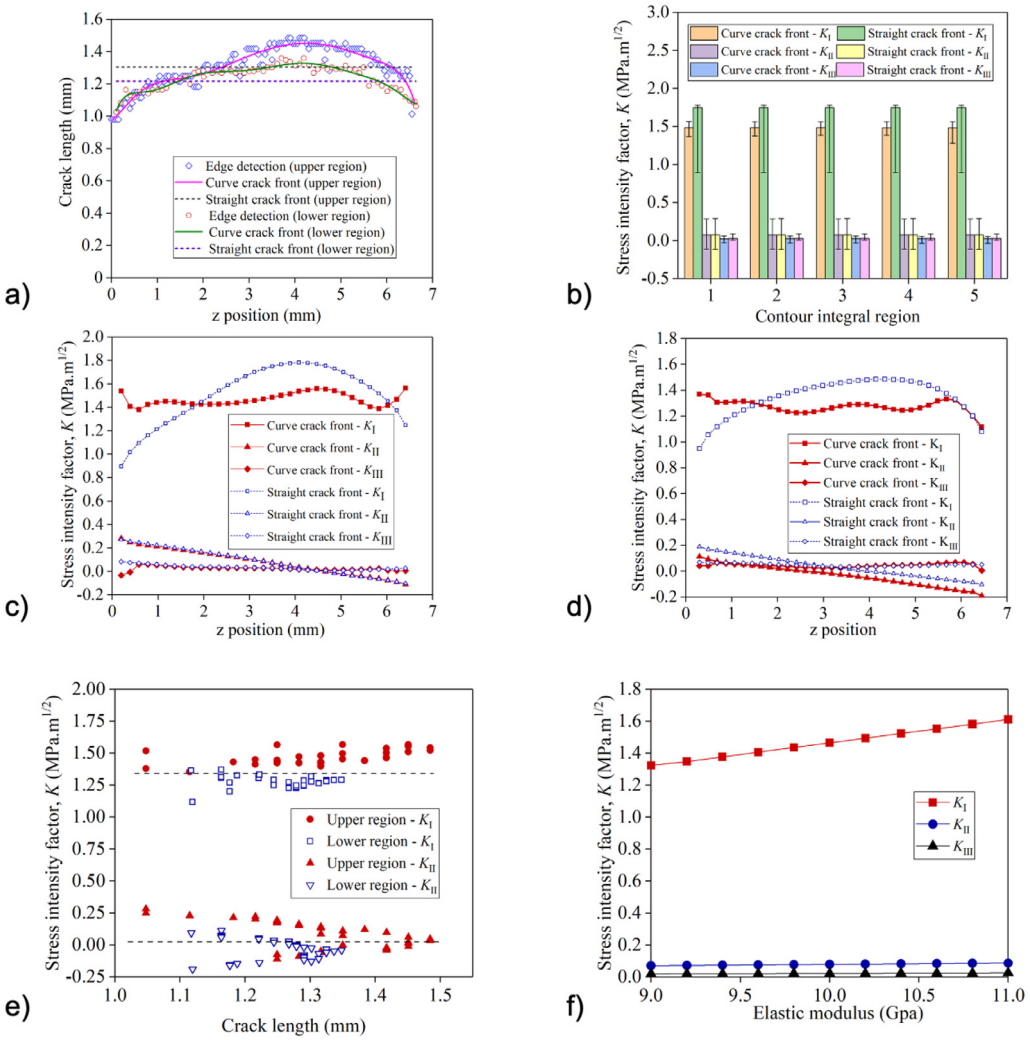

Fig. 9. Estimation of the fracture toughness in the FEM–(a) Crack fronts inserted into the FEM (upper and lower cracks); (b) K_I, K_{II} and K_{III} for different contour integral regions, with curved and straight crack fronts (upper crack); (c) Variation of K_I, K_{II} and K_{III} for the upper crack along the thickness direction; (d) Variation of K_I, K_{II} and K_{III} for the lower crack along the thickness direction; (e) Variation of K_I and K_{II} with local crack length (upper and lower cracks); (f) The effect of Young modulus on K_I, K_{II} and K_{III}, for the upper crack.

4. Conclusions

Testing of a fine-grained graphite specimen of SNG742 graphite in the DCDC geometry has been observed in situ by X-ray computed tomography. Digital volume correlation measured the resulting 3D displacement fields, which were used with a linear elastic FEM analysis to evaluate the Young modulus and three-dimensional stress intensity factors.

- A simple inverse analysis of the deformation before crack initiation estimated the elastic Young modulus at approximately 10 GPa.
- An edge detection algorithm applied to the DVC data provided an objective and reliable measure of the curved crack shape. The crack mouth opening varied in proportion with the local crack length, and the crack tip opening angle was constant across the crack front.
- The mode I stress intensity K_I along the tip of the curved crack was approximately constant, and provided a measure of the fracture toughness. The mode II and mode III stress intensity factors were negligible. The assumption of a straight crack of average length produced errors of 3% compared to the curved crack front.

Declaration of Competing Interest

The authors declare that they have no known competing financial interests or personal relationships that could have appeared to influence the work reported in this paper.

CRediT authorship contribution statement

Jie Shen: Formal analysis, Software, Writing – original draft. **T James Marrow:** Conceptualization, Methodology, Supervision, Writing – review & editing. **Daniel Scotson:** Investigation, Formal analysis. **Xiaochao Jin:** Investigation, Software. **Houzheng Wu:** Resources. **Hongniao Chen:** Funding acquisition, Investigation, Software, Supervision.

Acknowledgments

Jie Shen and H. Chen gratefully acknowledges the support of the National Natural Science Foundation of China (Grant No. 51768011) and the China Scholarship Fund (Award No. 201906675001) that enabled their participation in this work. The materials were provided by Houzheng Wu, Loughborough University and the test specimen was fabricated by Sinosteel Ltd. The X-ray microscope,

software and workstation used for the tomography and digital volume correlation analysis was supported by EPSRC Grant EP/M02833X/1 “University of Oxford: experimental equipment upgrade”.

References

[1] B.T. Kelly, Graphite–The most fascinating nuclear material, Carbon 20 (1982) 3–11.
[2] R. Taylor, R.G. Brown, K. Gilchrist, E. Hall, A.T. Hodds, B.T. Kelly, F. Morris, The mechanical properties of reactor graphite, Carbon 5 (1967) 519–531.
[3] M.C. Carroll, D.T. Rohrbaugh, P. Chakraborty, W.D. Swank, Evaluating alternate test techniques to characterize mechanical properties in nuclear-grade graphites, American Nuclear Society, Las Vegas, NV, United states, 2016, pp.269-275, Conference: HTR 2016: International Topical Meeting on High Temperature Reactor Technology, Las Vegas, NV (United States), 6-10 Nov 2016
[4] S. Mohanty, S. Majumdar, M. Srinivasan, Constitutive modeling and finite element procedure development for stress analysis of prismatic high temperature gas cooled reactor graphite core components, Nucl. Eng. Des. 260 (2013) 145–154.
[5] J. Sumita, Y. Shimazaki, T. Shibata, Investigation on structural integrity of graphite component during high temperature 950°C continuous operation of HTTR, J. Nucl. Sci. Technol. 51 (2014) 1364–1372.
[6] D. Tsang, B.J. Marsden, The development of a stress analysis code for nuclear graphite components in gas-cooled reactors, J. Nucl. Mater. 350 (2006) 208–220.
[7] V. Svalbonas, T.C. Stilwell, Z. Zudans, Rules for design of nuclear graphite core components–Some considerations and approaches, Nucl. Eng. Des. 46 (1978) 313–333.
[8] M.P. Hindley, D.C. Blaine, A.A. Groenwold, T.H. Becker, Failure prediction of full-size reactor components from tensile specimen data on NBG-18 nuclear graphite, Nucl. Eng. Des. 284 (2015) 1–9.
[9] J.A. Vreeling, O. Wouters, J. Laan, Graphite irradiation testing for HTR technology at the High Flux Reactor in Petten, J. Nucl. Mater. 381 (2008) 68–75.
[10] G. Haag, D. Mindermann, G. Wilhelmi, H. Persicke, W. Ulsamer, Development of reactor graphite, J. Nucl. Mater. 171 (1990) 41–48.
[11] S. Yu, X. Fang, H. Wang, C. Li, Failure probability study of HTR graphite component using microstructure-based model, Nucl. Eng. Des. 253 (2012) 192–199.
[12] Standard Test Method for Determination of Fracture Toughness of Graphite at Ambient Temperature, D7779-11R15, International, ASTM, 2015.
[13] M.C. Carroll, D.T. Rohrbaugh, P. Chakraborty, W.D. Swank, in: Evaluating alternate test techniques to characterize mechanical properties in nuclear–grade graphites, American Nuclear Society, Las Vegas, NV, United states, 2016, pp. 269–275. Conference: HTR 2016: International Topical Meeting on High Temperature Reactor Technology, Las Vegas, NV (United States), 6-10 Nov 2016.
[14] A. Tzelepi, P. Ramsay, A.G. Steer, J. Dinsdale-Potter, Measuring the fracture properties of irradiated reactor core graphite, J. Nucl. Mater. 509 (2018) 667–678.
[15] G. Pallares, L. Ponson, A. Grimaldi, M. George, G. Prevot, M. Ciccotti, Crack opening profile in DCDC specimen, Int. J. Fract. 156 (2009) 11–20.
[16] J. Wade-Zhu, R. Krishna, A.J. Bodey, M. Davies, N.K. Bourne, C. Rau, B. Davies, A. Tzelepi, A.N. Jones, B.J. Marsden, P.M. Mummery, 4D synchrotron X-ray microtomography of fracture in nuclear graphite after neutron irradiation and radiolytic oxidation, Carbon 168 (2020) 230–244.
[17] C. Janssen, Specimen for fracture mechanics studies on glass, Rev. Phys. Appl. 12 (1977) 803.
[18] M.Y. He, M.R. Turner, A.G. Evans, Analysis of the double cleavage drilled compression specimen for interface fracture energy measurements over a range of mode mixities, Acta Metall. Mater. 43 (1995) 3453–3458.
[19] W.E. Warren, Theoretical analysis of the double cleavage drilled compression specimen, Int. J. Fract. 33 (1987) 223–235.
[20] S.M. Barhli, L. Saucedo-Mora, M. Jordan, A.F. Cinar, C. Reinhard, M. Mostafavi, T.J. Marrow, Synchrotron X-ray characterisation of crack strain fields in polygranular graphite, Carbon 124 (2017) 357–371.
[21] S.M. Barhli, Advanced quantitative analysis of crack fields, observed by 2D and 3D image correlation, volume correlation and diffraction mapping, [PhD Thesis], University of Oxford, 2017 https://ora.ox.ac.uk/objects/uuid:d6240241-8a1e-4a8e-aff0-4a2ef14b0da7.
[22] X. Jin, J. Wade-Zhu, Y. Chen, P.M. Mummery, X. Fan, T.J. Marrow, Assessment of the fracture toughness of neutron-irradiated nuclear graphite by 3D analysis of the crack displacement field, Carbon 171 (2021) 882–893.
[23] S.M. Barhli, M. Mostafavi, A.F. Cinar, D. Hollis, T.J. Marrow, J-Integral calculation by finite element processing of measured full-field surface displacements, Exp. Mech. 57 (2017) 997–1009.
[24] H.H.N. Chen, R.K.L. Su, S.L. Fok, H.G. Zhang, Fracture behavior of nuclear graphite under three-point bending tests, Eng. Fract. Mech. 186 (2017) 143–157.
[25] T.H. Becker, T.J. Marrow, R.B. Tait, Damage, crack growth and fracture characteristics of nuclear grade graphite using the Double Torsion technique, J. Nucl. Mater. 414 (2011) 32–43.
[26] M. Mostafavi, Y. Vertyagina, C. Reinhard, R. Bradley, X. Jiang, M. Galano, J. Marrow, 3D studies of indentation by combined X-ray tomography and digital volume correlation, Key Eng. Mater. 592-593 (2013) 14–21.
[27] M. Mostafavi, D.M. Collins, B. Cai, R. Bradley, R.C. Atwood, C. Reinhard, X. Jiang, M. Galano, P.D. Lee, T.J. Marrow, Yield behavior beneath hardness indentations in ductile metals, measured by three-dimensional computed X-ray tomography and digital volume correlation, Acta Mater. 82 (2015) 468–482.
[28] M. Souza, L.C. Pardini, E.C. Botelho, M. Costa, X-ray tomography applied to the void/defect measurement of hybrid CFRC/SiC composites, Mater. Res. Express 6 (2018).
[29] T.J. Marrow, D. Liu, S.M. Barhli, L. Saucedo Mora, Y. Vertyagina, D.M. Collins, C. Reinhard, S. Kabra, P.E.J. Flewitt, D.J. Smith, In situ measurement of the strains within a mechanically loaded polygranular graphite, Carbon 96 (2016) 285–302.
[30] G. Liu, L. Wang, Y. Yi, L. Sun, S. Ma, Inverse identification of graphite damage properties under complex stress states, Mater. Des. 183 (2019) 108135.
[31] B.J. Marsden, G.N. Hall, in: Comprehensive Nuclear Materials, Elsevier Ltd, 2012, pp. 325–390.
[32] B.T. Kelly, T.D. Burchell, Structure-related property changes in polycrystalline graphite under neutron irradiation, Carbon 32 (1994) 499–505.
[33] E.D. Ea Son, G.N. Hall, B.J. Marsden, G.B. Heys, A model of Young's modulus for Gilsocarbon graphites irradiated in oxidising environments, J. Nucl. Mater. 436 (2013) 201–207.
[34] E.S. Kim, H.C. No, B.J. Kim, C.H. Oh, Estimation of graphite density and mechanical strength variation of VHTR during air-ingress accident, Nucl. Eng. Des. 238 (2008) 837–847.
[35] T. Arai, S. Sato, T. Oku, H. Schiffers, W. Delle, Assessment of heterogeneity and anisotropy of IG-110 graphite for nuclear components, J. Nucl. Sci. Technol. 28 (2008) 713–720.
[36] J.D. Arregui-Mena, L. Margetts, D.V. Griffiths, L. Lever, G. Hall, P.M. Mummery, Spatial variability in the coefficient of thermal expansion induces pre-service stresses in computer models of virgin Gilsocarbon bricks, J. Nucl. Mater. 465 (2015) 793–804.
[37] M.P. Metcalfe, N. Tzelepi, D. Wilde, Effect of test specimen size on graphite strength, symposium on graphite testing for nuclear applications–The significance of test specimen volume and geometry and the statistical significance of test specimen population, 2014, pp.1–29.
[38] L. Lin, H. Li, A.S.L. Fok, M. Joyce, J. Marrow, Characterization of heterogeneity and nonlinearity in material properties of nuclear graphite using an inverse method, J. Nucl. Mater. 381 (2008) 158–164.
[39] M.R. Joyce, T.J. Marrow, Microstructural scale strain localisation in nuclear graphite, J. Nucl. Mater. 381 (2008) 171–176.
[40] W. Lu, X. Li, X. Wu, L. Sun, Z. Li, Investigation on the oxidation behavior and multi-step reaction mechanism of nuclear graphite SNG742, J. Nucl. Sci. Technol. 57 (2019) 1–13.
[41] T.D. Burchell, D. Erdman, R.R. Lowden, J. Hunter, C. Hannel, The fracture toughness of nuclear graphite grades (ORNL/TM-2016/678), Oak Ridge National Lab. (ORNL), Oak Ridge, TN (United States), 2016.
[42] A.F. Cinar, S.M. Barhli, D. Hollis, M. Flansbjer, R.A. Tomlinson, T.J. Marrow, M. Mostafavi, An autonomous surface discontinuity detection and quantification method by digital image correlation and phase congruency, Opt. Laser Eng. 96 (2017) 94–106.
[43] L. Yan, A. Cinar, S. Ma, R. Abel, T.J. Marrow, A method for fracture toughness measurement in trabecular bone using computed tomography, image correlation and finite element methods, J. Mech. Behav. Biomed. Materials 109 (2020) 103838.
[44] L. Li-jun, Y. Ying, H. Ming-ge, Y. Xiang-yun, Edge detection algorithm of magnetic tile crack based on wavelet modulus maxima, J. Univ. Electron. Sci. Technol. China 44 (2015) 283–288.
[45] F. Yan-Jun, W. Xiao-Hong, L. Dai-sheng, A modified image edge detection algorithm based on wavelet transform, J. Sichuan Univ. 49 (2012) 96–100 (in Chinese).